The POTRA domains of Toc75 exhibit chaperone-like function to facilitate import into chloroplasts

Patrick K. O'Neil[a,b,1], Lynn G. L. Richardson[c,1], Yamuna D. Paila[c], Grzegorz Piszczek[d], Srinivas Chakravarthy[e], Nicholas Noinaj[a,b,2], and Danny Schnell[c,2]

[a]Markey Center for Structural Biology, Department of Biological Sciences, Purdue University, West Lafayette, IN 47907; [b]Purdue Institute of Inflammation, Immunology and Infectious Disease, Purdue University, West Lafayette, IN 47907; [c]Department of Plant Biology, Michigan State University, East Lansing, MI 48824; [d]National Heart, Lung, and Blood Institute, National Institutes of Health, Bethesda, MD 20892; and [e]Biophysics Collaborative Access Team, Illinois Institute of Technology, Sector 18ID, Advanced Photon Source, Argonne National Laboratory, Lemont, IL 60439

Edited by Kenneth Keegstra, Michigan State University, East Lansing, MI, and approved May 8, 2017 (received for review December 23, 2016)

Protein trafficking across membranes is an essential function in cells; however, the exact mechanism for how this occurs is not well understood. In the endosymbionts, mitochondria and chloroplasts, the vast majority of proteins are synthesized in the cytoplasm as preproteins and then imported into the organelles via specialized machineries. In chloroplasts, protein import is accomplished by the TOC (translocon on the outer chloroplast membrane) and TIC (translocon on the inner chloroplast membrane) machineries in the outer and inner envelope membranes, respectively. TOC mediates initial recognition of preproteins at the outer membrane and includes a core membrane channel, Toc75, and two receptor proteins, Toc33/34 and Toc159, each containing GTPase domains that control preprotein binding and translocation. Toc75 is predicted to have a β-barrel fold consisting of an N-terminal intermembrane space (IMS) domain and a C-terminal 16-stranded β-barrel domain. Here we report the crystal structure of the N-terminal IMS domain of Toc75 from *Arabidopsis thaliana*, revealing three tandem polypeptide transport-associated (POTRA) domains, with POTRA2 containing an additional elongated helix not observed previously in other POTRA domains. Functional studies show an interaction with the preprotein, preSSU, which is mediated through POTRA2-3. POTRA2-3 also was found to have chaperone-like activity in an insulin aggregation assay, which we propose facilitates preprotein import. Our data suggest a model in which the POTRA domains serve as a binding site for the preprotein as it emerges from the Toc75 channel and provide a chaperone-like activity to prevent misfolding or aggregation as the preprotein traverses the intermembrane space.

protein import | chloroplast | outer membrane | Toc75 | POTRA domain

Chloroplasts, like mitochondria, are organelles of endosymbiotic origin, having evolved from initial engulfment of a cyanobacterium by a eukaryotic cell (1–3). Following endosymbiosis, massive gene transfer from the cyanobacterial ancestral genome to the nuclear genome of the host necessitated a mechanism for protein transport back into the organelle, where these proteins perform their functions (4). The efficient targeting and translocation of proteins into chloroplasts and other plastid types is essential for plant growth and development. In plants, the majority of chloroplast proteins that are encoded in the nucleus are translated in the cytosol with an N-terminal transit peptide, which facilitates their translocation into chloroplasts. Protein import is mediated by the translocons at the outer chloroplast (TOC) and inner chloroplast (TIC) envelopes (5). The major components of the TOC machinery include the preprotein receptors Toc159 and Toc33 (Toc34 in pea), which are membrane-bound GTPases, and Toc75, a β-barrel protein that forms a cation-selective channel through which preproteins cross the outer membrane (6–8). Toc75 also is implicated in the insertion of outer membrane proteins that lack an N-terminal transit peptide (9, 10). An additional TOC complex component, Toc64, has a tetratricopeptide repeat domain and serves as a receptor site for cytosolic Hsp90/70 and their chloroplast-bound substrates (11, 12).

Toc75 belongs to the Omp85 superfamily of β-barrel integral membrane proteins found in Gram-negative bacteria, as well as in mitochondria and chloroplasts (13). In addition to Toc75, chloroplasts have an additional Omp85 family member, outer envelope protein 80 (OEP80). OEP80 is not found associated with core TOC/TIC complex components (14, 15), and has diverged significantly in sequence from Toc75 (16, 17), implying that it is not involved in protein import. The function of OEP80 remains unknown; however, it is essential for plant viability (18). Omp85 family members are found exclusively in the outer membranes of Gram-negative bacteria, chloroplasts, and mitochondria and have critical roles in outer membrane protein biogenesis and protein transport (19–22). This family includes β-barrel assembly machinery protein A (BamA) in Gram-negative bacteria (23), and sorting and assembly machinery of 50 kDa (Sam50) in mitochondria (24).

BamA is a component of the β-barrel assembly machinery (BAM), which is involved in the biogenesis of β-barrel outer membrane proteins. Sam50, a component of the mitochondrial sorting and assembly machinery (SAM), functions in insertion of nascent β-barrel membrane proteins into the mitochondrial outer membrane. Characteristic features shared by proteins of this family are membrane-integrated β-barrel and soluble polypeptide-transport associated (POTRA) domains that, although divergent in amino acid sequence, retain an evolutionarily conserved fold

Significance

Nearly all proteins found within chloroplasts are synthesized in the cytoplasm as preproteins and then imported and trafficked to their final destination. The initial steps in importation are orchestrated by the TOC complex, which includes Toc75, serving as the translocation channel, and Toc33 and Toc159, both containing GTPase domains, which help drive substrate selection and importation. Aside from the soluble domain of Toc33/34, structural information for the TOC complex is lacking, hindering our ability to form mechanistic models for function. Here we report a structure of Toc75 consisting of three tandem POTRA domains. Our findings indicate that the POTRA domains may help facilitate preprotein import by directly binding preproteins and orchestrating handoff to the TIC complex.

Author contributions: Y.D.P., N.N., and D.S. designed research; P.K.O., L.G.L.R., G.P., S.C., and N.N. performed research; P.K.O., L.G.L.R., G.P., S.C., N.N., and D.S. analyzed data; and P.K.O., L.G.L.R., N.N., and D.S. wrote the paper.

The authors declare no conflict of interest.

This article is a PNAS Direct Submission.

Data deposition: Structure factors and model coordinates have been deposited in the Protein Data Bank, www.pdb.org (PDB ID codes 5UAY and 5UBC).

[1]P.O. and L.G.L.R. contributed equally to this work.

[2]To whom correspondence may be addressed. Email: nnoinaj@purdue.edu or schnelld@msu.edu.

This article contains supporting information online at www.pnas.org/lookup/suppl/doi:10.1073/pnas.1621179114/-/DCSupplemental.

www.pnas.org/cgi/doi/10.1073/pnas.1621179114

of $\beta_1\alpha_1\alpha_2\beta_2\beta_3$ structural motifs (25). BamA, one of the most well-characterized member of this family, has five POTRA domains residing in the periplasm, where they interact with nascent outer membrane protein substrates (23, 26), additional components of the BAM complex (Bam B–E), and the periplasmic chaperone, SurA (27). It also has been suggested recently that the BamA POTRAs are involved in modulating the conformation of the BamA β-barrel to promote the insertion of nascent outer membrane proteins (28). In mitochondria, Sam50 is oriented with its single POTRA domain within the intermembrane space (IMS), where it interacts with substrates and promotes their release from Sam50 (29). It also interacts with the mitochondrial inner membrane organizing system, a large protein complex at the mitochondrial inner membrane that maintains inner membrane architecture (30). Study of the individual members of this protein family has shown that the POTRA domains have unique but critical roles in the proper function and assembly of these protein targeting/integration machineries.

Toc75 has three POTRA domains that reside in the chloroplast IMS (15, 31). Recent studies have shown that all three POTRAs are essential for viability, because removal of a single POTRA domain resulted in failure to complement the lethal *Arabidopsis toc75* null mutant (15, 32–34). Moreover, expression of serial deletions of each POTRA domain resulted in dominant-negative phenotypes (15). Molecular characterization of these mutants indicated a role for the POTRAs in early stages of chloroplast preprotein translocation through the TOC complex and in proper assembly of TOC complexes (15). Furthermore, Toc75 POTRAs interact with precursor proteins and the intermembrane space chaperone Tic22 in direct binding studies.

To better understand how Toc75 has adapted to perform a unique function in chloroplast protein translocation, and given the functional importance of the POTRA domains of Toc75 and other Omp85 family members, we solved the crystal structure of the three POTRA domains of Toc75. The structure reveals that the POTRA domains form an L-shaped structure very similar to BamA, with a unique extended helix within POTRA2 that is not observed in the POTRA domains of BamA and other Omp85 family members (25, 28, 35–38). Based on these unique structural properties, we investigated the contribution of individual POTRA repeats in binding chloroplast precursors. We found that the POTRA domains have chaperone-like activity, attributed mainly to POTRA2-3. These results support a model in which the POTRA domains act to bind and chaperone preproteins as they emerge from the TOC channel into the IMS, and function in conjunction with the IMS chaperone Tic22 to prevent precursor misfolding or aggregation during protein import.

Results

Crystal Structure of the POTRA Domains of Toc75. For structural and biophysical studies, the Toc75 sequence from *Aribidopsis thaliana* was codon-optimized (Bio Basic), and the three POTRA domains (residues 141–449; POTRA1-3) were subcloned into the pHIS-parallel2 vector containing an N-terminal 6×-His tag, followed by a tobacco etch virus (TEV) protease site (Fig. 1*A*). Expression into natively folded protein was unsuccessful; however, refolding from urea-solubilized inclusion bodies using a slow dialysis method was successful and produced sufficient quantities for biophysical characterization to confirm proper folding. The refolded sample was further purified on a Ni-NTA column, and the 6×-His tag was removed by TEV protease treatment. The elution profile on an S200 size-exclusion column showed a monodispersed species that ran at ~38 kDa on SDS/PAGE (Fig. 1 *B* and *C*). Sedimentation velocity analytical ultracentrifugation showed predominantly monomeric species (~90%), with only traces of dimer species (Fig. 1*D*). To provide further confirmation of proper folding of the refolded sample, we next used size-exclusion chromatography small-angle X-ray scattering (SEC-SAXS) to determine the scattering properties, which produced an R_g value of ~27 Å with a D_{max} value of ~100 Å, both of which are consistent with a model of three tandem POTRA domains from *Escherichia coli* (26, 39, 40) (Fig. 1 *E* and *F*).

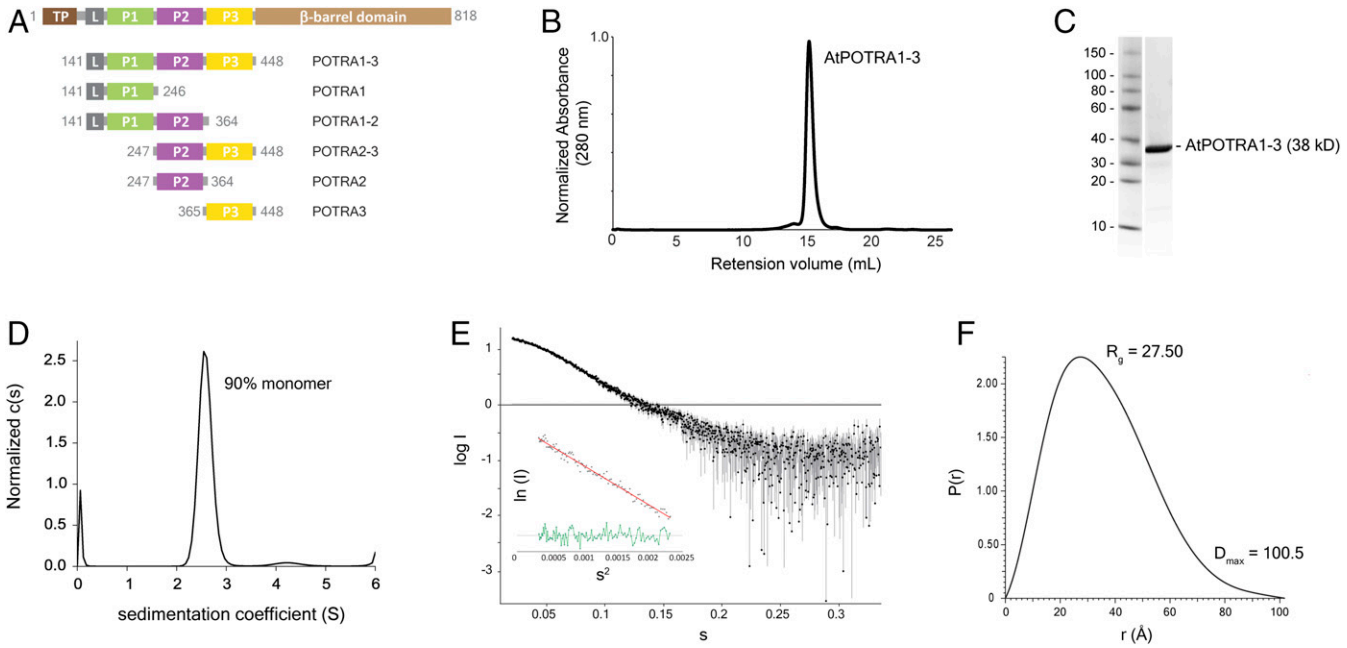

Fig. 1. Biophysical characterization of refolded POTRA1-3 of *At*Toc75. (*A*) Construct design of *A. thaliana* Toc75 POTRA domains analyzed in this study. (*B*) Size exclusion chromatography elution profile for refolded POTRA1-3 showing a sharp Gaussian peak eluting ~15.5 mL on a Superdex S200 Increase 10/300 GL column. (*C*) SDS/PAGE analysis of purified POTRA1-3 running at ~38 kDa. (*D*) Sedimentation velocity experiments using analytical ultracentrifugation showing that the refolded POTRA1-3 is almost exclusively monomer. (*E*) SAXS curve of refolded POTRA1-3 with an *s* range of 0.007–0.35. (*Inset*) The Guinier plot (red line with black dots) with residuals (green line). (*F*) The pair distribution function, P(r), for POTRA1-3 yielding an R_g of 27.50 Å and a D_{max} of 100.5 Å.

Broad matrix crystallization screening produced several initial lead conditions in two crystal forms, which were further optimized with the best crystals growing for ~3 d at 12 °C in 100 mM Mes pH 5.0 and 10% PEG 6000 (space group $P2_1$) and 100 mM Hepes:NaOH pH 7.5 and 20% PEG 8000 (space group $P2_12_12_1$). Data were collected at the Southeast Regional Collaborative Access Team (SER-CAT) 22-ID beamline at the Advanced Photon Source, Argonne National Laboratory, with data used for experimental phasing collected at beamline 8.2.2 at the Advanced Light Source, Lawrence Berkeley National Laboratory. The initial structure was determined by selenium single-wavelength anomalous dispersion (Se-SAD) phasing using AutoSol in PHENIX, and the subsequent structures were determined by molecular replacement, with refinement performed using phenix.refine and model building done in Coot. The POTRA1-3 structure was determined in two different space groups, $P2_12_12_1$ solved to 2.5-Å resolution and $P2_1$ solved to 2.85-Å resolution, which produced nearly identical structures (Table S1).

The structures contain residues 148–448 of Toc75, including the N-terminal linker and all three POTRA domains. The N-terminal linker (residues 148–172) caps the end of POTRA1. The overall structure of POTRA1-3 has a bent L-shaped conformation in which POTRA1 and POTRA3 fold into one another, each containing the conserved core βααββ fold seen in other POTRA domains solved to date (Fig. 2 *A*–*C*). Although POTRA2 also has the conserved core fold, it contains a 40-residue insertion that folds into an elongated α-helix (P2-helix) and loop, producing an overall βαααββ fold. This fold is most clearly seen when the three POTRAs are superimposed (Fig. 2*C*). This α-helix insertion is unique to Toc75 and is not observed in BamA, Sam50, or OEP80 (17). The previously identified flanking cysteine residues (C256 and C300) were found in proximity to each other and ideally positioned to form a potential disulfide in vivo in the unstructured loop adjacent to the P2-helix, which may further stabilize the overall structure (17) (Fig. 2*D*). The bent conformation for Toc75 POTRA1–-3 most closely resembles that of POTRA3-5 of BamA, which sit adjacent to the β-barrel domain, yet whether it is as flexible remains to be determined (Fig. 2*E*). An electrostatic surface potential map shows a number of charged patches, including a large electronegative region along the P2-helix, and two large electropositive regions along both POTRA1 and POTRA3 (Fig. 2*F*). A number of lipophilic (hydrophobic) patches were observed across the entire structure, particularly along POTRA2 (Fig. 2*G*). The crystal structure for POTRA1-3 was then fitted into a molecular envelope calculated from the SEC-SAXS data, showing good agreement and a nice fit of the experimental and calculated scattering curves, providing further evidence that the crystal structure accurately represents the structure found in solution (Fig. 2 *H* and *I*).

POTRA2-3 Mediates an Interaction with the Model Chloroplast Preprotein preSSU. It was previously observed that POTRA1-3 interacts with the chloroplast precursor of the small subunit of Rubisco (preSSU) (15, 17, 41) in an in vitro solid-phase binding assay. The localization of the POTRA domains in the intermembrane space led to the proposal that they serve as docking sites for the preprotein as it is transported across the outer membrane (15, 31). We wanted to investigate the contributions of individual POTRA domains to the interaction with preSSU given the unique structural features of the Toc75 POTRA domains relative to BamA (Fig. 2*E*). We were particularly interested in determining the role of POTRA2 because of its unusual P2-helix and prevalent hydrophobic patches. To this end, we generated constructs corresponding to individual or combinations of the POTRA domains, as shown in Fig. 1*A*. The POTRA constructs were expressed in *E. coli*, stably refolded, and immobilized on Ni-NTA beads via His_6 tags.

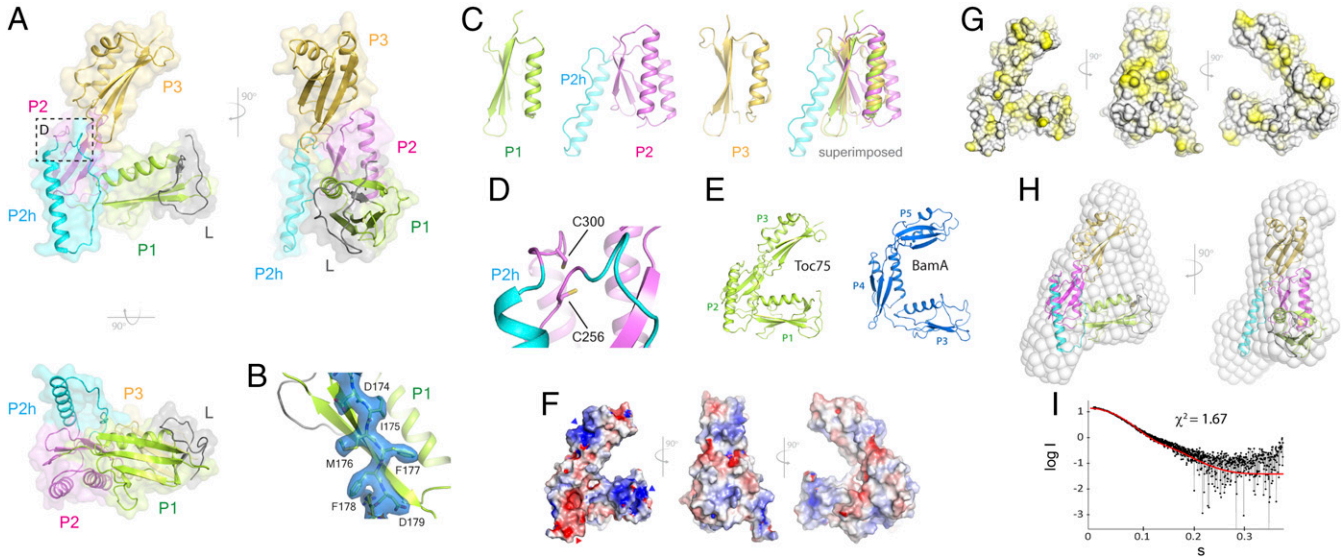

Fig. 2. The crystal structure of POTRA1-3 of *At*Toc75. (*A*) Orthogonal views of the structure of POTRA1-3 from *At*Toc75 with the N-terminal linker (L) shown in gray, POTRA1 (P1) shown in green, POTRA2 (P2) shown in magenta with the P2-helix (P2h) in cyan, and POTRA3 (P3) shown in gold. (*B*) Representative electron density ($2F_o - F_c$ map, 1.0 σ) shown as a blue isosurface for the POTRA1-3 structure along residues 174–179. (*C*) Comparison of the individual POTRA domains of POTRA1-3 to one another, highlighting the conserved overall fold and the P2-helix insertion (cyan). (*D*) Zoomed region indicated by the dashed box in *A*. The P2-helix flanking cysteine residues 256 and 300 are close to one another and ideally positioned for disulfide formation in vivo or in absence of reductant. (*E*) The overall fold of POTRA1-3 (green) most closely resembles that of POTRA3-5 of *E. coli* BamA (blue). (*F*) Orthogonal views of the electrostatic surface potential (±5 kT/e), with red indicating strongly electronegative and blue indicating strongly electropositive regions. Blue triangles indicate two electropositive regions, and the red triangle indicates an electronegative region. (*G*) Orthogonal views of the lipophilic potential of the POTRA1-3 structure mapped to the surface, with regions of high lipophilic potential (hydrophobicity) shown in yellow. (*H*) Crystal structure of POTRA1-3 fitted into the SAXS ab initio molecular envelope. (*I*) Comparison of the experimental scattering curve (gray) to the calculated scattering curve (red line) from the crystal structure with a χ^2 value of 1.67.

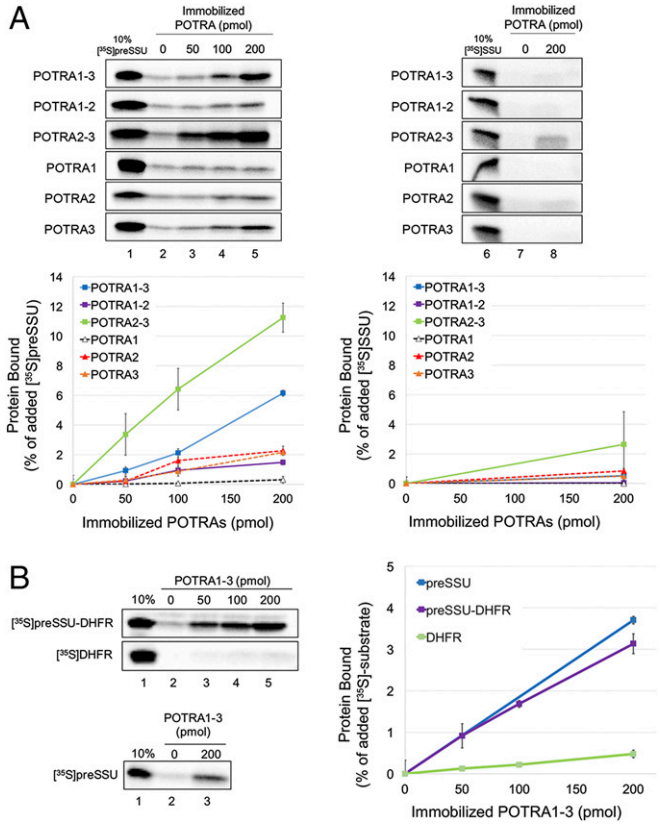

Fig. 3. Interaction of POTRA domains with preSSU. (*A*) Increasing amounts of POTRA-derived bait, as indicated, were immobilized on 10 μL of Ni-NTA resin and incubated with equimolar amounts of [^{35}S]SSU or [^{35}S]preSSU, respectively. Bound protein was eluted in SDS/PAGE sample buffer containing 0.5 M imidazole and resolved by SDS/PAGE. Phosphorimages of eluted [^{35}S]SSU and [^{35}S]preSSU are shown in the top panels. Lanes 1 and 6 contain 10% of [^{35}S]preSSU or [^{35}S]SSU added to the reaction, respectively. Signal intensity within bands corresponding to eluted [^{35}S]preSSU or [^{35}S]mSSU from triplicate experiments were quantitated with subtraction of background binding to resin (~1–3%, lanes 2 and 7), and plotted as a percentage of the total [^{35}S]preSSU added to the initial reaction. (*B*) Same as in *A*, testing the interaction between POTRA1-3 and either the transit peptide of preSSU fused to DHFR ([^{35}S]preSSU-DHFR) or [^{35}S]DHFR.

We tested the interactions of the constructs with equimolar concentrations of the [^{35}S]preSSU preprotein or [^{35}S]SSU lacking a transit peptide in solid-phase binding assays. Binding of [^{35}S]preSSU and [^{35}S]SSU was quantified from triplicate experiments after subtracting the background binding of the radiolabeled proteins to the Ni-NTA beads alone (ranging from 0.9% to 2.8%; lanes 2 and 7). POTRA1-3 and POTRA2-3 both bound to [^{35}S]preSSU in a dose-dependent manner (Fig. 3*A*) (15, 41). The other POTRA truncations showed minimal binding to [^{35}S]preSSU above background levels (Fig. 3*A*). We conclude that POTRA2-3 forms the minimal preprotein binding site, and that individual domains are insufficient to account for the preprotein binding characteristics of this region (Fig. 3*A*).

No significant binding was observed between [^{35}S]SSU, which lacks a transit peptide, and any of the POTRA constructs (all less than ~3% of the total [^{35}S]SSU added) (Fig. 3*A*). This result suggests that the interaction of preSSU with POTRA1-3 and POTRA2-3 is dependent on the presence of the transit peptide. To test this, we investigated the interaction between POTRA1-3 and the transit peptide of preSSU fused to stably folded dihydrofolate reductase ([^{35}S]preSSU-DHFR) or [^{35}S]DHFR alone (Fig. 3*B*). As shown in Fig. 3*B*, POTRA1-3 interacted with preSSU-DHFR, but not with DHFR in a dose-dependent manner indistinguishable from the binding observed with [^{35}S]preSSU. Taken together, these results indicate that the Toc75 POTRA domains form a preprotein binding site, and that binding is mediated, at least in part, by an interaction with the preprotein transit peptide.

POTRA2-3 Exhibits Chaperone-Like Activity. The observation that the Toc75 POTRAs interact with preSSU suggested two possibilities for their function in the intermembrane space. The POTRA domains could act as a specific transit peptide-binding site for preproteins as they emerge from the β-barrel channel. Alternatively, or additionally, they could bind to unfolded regions of preproteins to prevent misfolding and thereby provide chaperone-like activity. The preference for binding to preSSU and preSSU-DHFR over SSU and DHFR is consistent with a transit peptide selectivity.

To test the possibility of a general chaperone-like activity, we performed an in vitro aggregation assay using insulin as a model substrate. In this assay, insulin B aggregation is induced by the reduction of A chain-B chain disulfide bonds with 20 mM DTT, and aggregation is measured over time by light scattering at 360 nm (42). In our system, chaperone activity was assessed by the ability of the added POTRAs to prevent B chain aggregation and the resulting reduction in light scattering. Full-length POTRA1-3 was tested in the aggregation assay at a range of molar ratios to insulin. As shown in Fig. 4*A*, incubation of insulin with POTRA1-3 at a molar ratio of 1:1 showed a small reduction in insulin aggregation (~20%); however, at an insulin: POTRA1-3 molar ratio of 1:2, a ~70% reduction in insulin aggregation was observed at the latest time point tested. POTRA2-3 exhibited chaperone activity nearly identical to that of POTRA1-3, with a 20% reduction in insulin aggregation at a 1:1 molar ratio and a >60% reduction at a 1:2 molar ratio (Fig. 4*C*). POTRA1-2 showed a modest reduction in insulin aggregation of ~40% (Fig. 4*B*) at a molar ratio of 1:2. POTRA1 alone showed no chaperone activity at either a 1:1 or a 1:2 molar ratio (Fig. 4*D*). POTRA2 and POTRA3 were not tested, because neither of these domains individually contributed to precursor binding (Fig. 3*A*). Taken

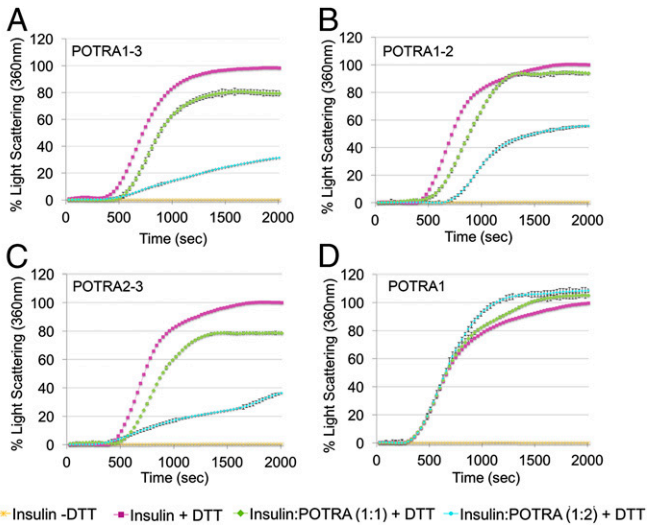

Fig. 4. Chaperone-like activity of the POTRA domains. Insulin was incubated with full-length POTRAs (POTRA1-3) (*A*), POTRA1-2 (*B*), POTRA2-3 (*C*), or POTRA1 (*D*) at an insulin:POTRA ratio of 1:1 or 1:2 as indicated. Insulin B aggregation was induced by the addition of 20 mM DTT. Aggregation was assessed by measuring light scattering at 360 nm, and is shown as a percentage of insulin aggregation in the presence of DTT and the absence of POTRAs (insulin + DTT). As a negative control, light scattering at 360 nm was also measured for insulin in the absence of DTT (Insulin − DTT).

together, these results demonstrate that the Toc75 POTRA domains have chaperone-like activity, and that this activity is attributed largely to POTRA2-3. These data are consistent with the findings of our preprotein-binding studies (Fig. 3) and suggest that the POTRAs function to provide both a preprotein binding site and chaperone activity in the intermembrane space.

Discussion

Protein import into chloroplasts is mediated by the TOC complex, with Toc75 serving as the central channel of the core translocon (5, 8). Although structures have been reported for the orthologs of the Omp85 family, including FhaC, TamA, and BamA, in Gram-negative bacteria (35, 36, 43–46), no structure has been reported for either Sam50 in mitochondria or Toc75 or OEP80 in chloroplasts. Here we report the structure of Toc75, from *A. thaliana*, consisting of the N-terminal linker and three tandem POTRA domains (Figs. 1*A* and 2*A*), and show that POTRA2-3 is critical for binding to chloroplast protein import substrate and also has intrinsic chaperone-like activity.

Our biophysical characterization confirms that POTRA1-3 is monomeric and the X-ray crystal structure closely corresponds with the SEC-SAXS solution structure. The overall structure was found in a bent L-shaped conformation, closely resembling that of POTRA3-5 of *E. coli* BamA (26, 39, 40). All three POTRA domains contained the conserved βααββ fold observed in other POTRA domains with relatively good structural alignment (23, 47, 48). Interestingly, the previously observed ∼40-residue insertion within Toc75 POTRA2 (17) overlaps with an extended α-helix encompassing residues 275–296, which we refer to as the P2-helix. This helix is not found in any of the BamA POTRAs (26, 36, 40) or POTRAs from Omp85 family members in the cyanobacteria *Nostoc* sp. PCC7120 and *Thermosynechoccocus*, both of which have structures available (17, 49, 50). In addition, based on sequence comparison, the insertion is unique to Toc75 relative to OEP80 and mitochondrial Sam50 (17).

Day et al. (17) previously investigated the conservation of the Toc75 POTRA domains in plant species. The *Arabidopsis* Toc75 POTRA domains used in this study exhibited >61% sequence identity to TOC75 proteins from across the land plants, including the bryophytes (e.g., *Physcomitrella patens*) and vascular plants (17). This conservation includes the residues that form the P2-helix, the large electropositive regions along both POTRA1 and POTRA3 (Fig. 2*F*), and the hydrophobic patches found along POTRA2 (Fig. 2*G*). Although Toc75 proteins from green and red algae also are predicted to contain three POTRA domains based on secondary structure predictions, the available algal sequences are highly divergent from those in land plants, as noted previously (17), and the lack of structural information for these proteins makes it difficult to determine whether the conserved charged and hydrophobic regions in land plants are present. Nonetheless, the P2-helix insertion is clearly absent from available algae sequences, and it was previously speculated that the P2-helix is an evolutionary adaptation of Toc75 in land plants (17, 25).

The P2-helix is flanked by two previously identified cysteine residues that were reduced in our structure; however, it can be rationalized that these cysteines may form a disulfide bond in vivo or in the absence of reductant, which would further stabilize the conformation of the P2-helix. Previous studies have implicated redox as a possible control mechanism for protein import at the level of the TOC complex, but the exact components contributing to this potential regulation are not known (51). It will be of considerable interest to determine whether C256 and C300 contribute to this function. Indeed, the cysteine residues flanking the P2-helix are also conserved in higher plants. Analysis of the electrostatic properties of the POTRA1-3 structure shows a number of charged hotspots for each of the POTRA domains, including two electropositive regions along POTRA1 and POTRA3 and one electronegative region along the P2-helix of POTRA2 (Fig. 2*F*). Importantly, the lipophilic properties show reasonably well-distributed hydrophobic patches across the entire surface (Fig. 2*G*). Together, these electrostatic and lipophilic properties may contribute to the role of POTRA1-3 in interacting with preproteins and its chaperone-like function (15).

Recent X-ray crystallography and cryo-EM studies reported the structures of several Omp85 family members, including FhaC, TamA, and BamA (28, 36–38, 43–47). Given the conservation of key features, these structures serve as models for Toc75, albeit with low sequence identity (7%, 7%, and 8%, respectively). Whereas TamA and BamA have roles in the biogenesis of β-barrel outer membrane proteins in Gram-negative bacteria (23, 52–55), FhaC has a role in the secretion of filamentous hemagglutinin (FHA) out of *Bordetella pertussis* (56). Here FhaC serves as the translocon within the outer membrane, first interacting with FHA via its TPS domain and then translocating FHA through its barrel domain, across the outer membrane, and into the extracellular milieu.

Given that the functional role of FhaC most closely matches that of Toc75, we used it as a scaffold for preparing an improved model for full-length Toc75 (Fig. 5 *A*–*C* and Dataset S1). POTRA2 of FhaC aligns surprisingly well with POTRA3 of Toc75, with an rmsd of ∼2.5 Å. In this model, the P2-helix is positioned away from the barrel domain. Previous studies have implicated POTRA2 in the assembly of the trimeric TOC complex by mediating interactions of Toc75 with the TOC GTPase receptors, with plants expressing Toc75 that lack POTRA1-2 (Toc75ΔP1-2) showing an increase in unassembled Toc33 in the chloroplast envelope as determined by blue-native PAGE. Toc159 also appears to be absent from complexes containing Toc75ΔP1-2 (15). In our model, the P2-helix is positioned to interact with regions of the TOC receptors that may be exposed to the intermembrane space side of the envelope, for example, the large membrane-protected domain of Toc159 or the short C-terminal tail of Toc33.

We previously demonstrated that POTRA1-3 binds chloroplast preproteins (15), and in the present study we show that this interaction is mediated by POTRA2-3. As with POTRA1-3, POTRA2-3 can bind transit peptides directly, consistent with a specific docking site for the targeting signal in the intermembrane space. We also demonstrate that POTRA2-3 has a chaperone-like activity that prevents insulin aggregation (Fig. 4). This finding reveals a second, previously undescribed activity of the POTRAs that could serve to prevent misfolding or aggregation of preproteins during translocation. Whether transit peptide binding and the chaperone-like activity of POTRA2-3 are independent functions remains to be determined. We cannot rule out the possibility that the chaperone-like activity of the POTRAs favors binding to transit peptides owing to their intrinsic structural instability (57–59). Although the overall structure of the Toc75 POTRAs is similar to that of POTRA3-5 of BamA, it is difficult to draw direct parallels between the two in terms of function. Toc75 substrates are physically quite different from those of BamA; chloroplast transit peptides are largely unstructured or α-helical in a membrane-mimicking environment (57–59), whereas β-strands are the main structural elements of BamA β-barrel substrates. In the case of BamA, it has been hypothesized that the POTRA domains provide a track on which the β-strands of incoming unfolded substrates align during insertion into the outer membrane via a process known as β-augmentation, in effect acting as a chaperone to incoming substrates (26, 39, 60). In an analogous way, as substrates exit the Toc75 channel in the intermembrane space during chloroplast protein import, they bind to POTRA2-3. This interaction could serve two functions. First, it would facilitate unidirectional translocation of the preprotein by preventing the preprotein from slipping back through the channel and into the cytoplasm. Second, the POTRA2-3 chaperone activity would prevent the preprotein from misfolding in the intermembrane space before engaging the

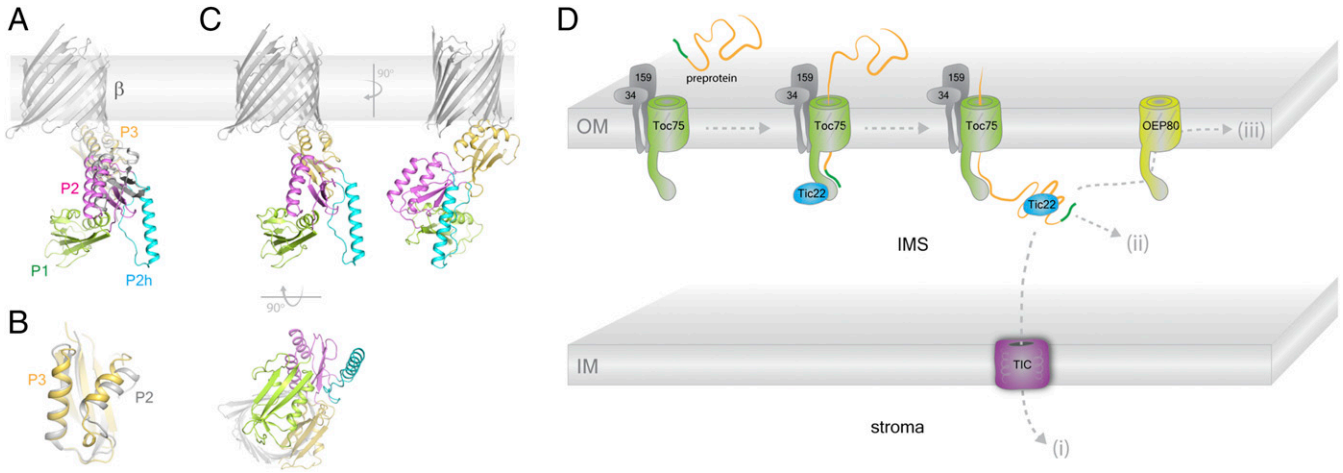

Fig. 5. Model for full-length *At*Toc75 and its role in the import of preproteins. (*A*) Superposition of FhaC (gray) and Toc75 POTRA1-3 aligned along POTRA2 (P2) of FhaC and POTRA3 (P3) of Toc75. (*B*) Zoomed view of the alignment along P2 of FhaC and P3 of Toc75, indicating their structural conservation with an rmsd of ~2.5 Å. (*C*) Orthogonal views of the structural model for full-length Toc75 consisting of the barrel domain of FhaC with the POTRA domains of Toc75 reported here. (*D*) Summary model for the role of the POTRA domains of Toc75 in the transport of precursor proteins into the IMS. Our work shows the POTRA domains may serve to help facilitate preprotein import by directly binding preproteins and orchestrating handoff to the TIC complex (*i*), the IMS (*ii*), or OEP80 (*iii*).

TIC complex. The structure of Toc75 POTRA1-3 has several features that may provide clues as to how POTRA2-3 acts as a chaperone; for example, several hydrophobic patches are observed within the structure, most notably within POTRA2 (Fig. 2*G*), and a large electronegative patch is seen on the P2-helix (Fig. 2*F*).

In a previous study, we also demonstrated that the Toc75 POTRAs bind Tic22, an import component in the intermembrane space (15, 61–63). Tic22 from the apicomplexan *Toxoplasma gondii* has been shown to have chaperone-like activity in vitro (42), suggesting that Tic22 also may act as an IMS chaperone for translocating precursors in chloroplasts. Mutants lacking both Tic22 homologs in *Arabidopsis* are import-deficient, and it was recently shown that Tic22 protein levels are up-regulated in plants expressing POTRA-deleted versions of Toc75 (15). Thus, it is likely that both the POTRA domains and Tic22 act as chaperones during protein import into the chloroplast. This suggests that the chaperone-like activities of the POTRA domains and Tic22 function in coordination to facilitate passage of the preprotein through the IMS.

Interestingly, POTRA1 alone does not appear to contribute significantly to the preprotein binding or chaperone activity of the POTRAs. In a previous study, we showed that deletion of POTRA1 resulted in significant dominant-negative effects when expressed in *Arabidopsis* (15). The POTRAs have multiple roles in TOC function in addition to preprotein binding, including TOC complex assembly and Tic22 binding (15). Toc75 also has a role in targeting and insertion of the TOC receptors and other proteins at the outer membrane (9, 10). Thus, it is possible that POTRA1 participates in these essential activities of the import channel.

Taken together, our present findings lead us to propose a model in which the POTRA domains of Toc75 facilitate the import of preproteins across the outer membrane by directly interacting with the preproteins as they exit the barrel domain (Fig. 5*D*). We hypothesize that the POTRA domains serve as binding sites for the transit peptides and provide chaperone-like activity to prevent misfolding or aggregation as the preproteins traverse the intermembrane space. The previously established interaction of the POTRAs with Tic22 might facilitate subsequent transfer of the preproteins to the TIC complex at the inner envelope membrane, transfer to OEP80 for insertion into the outer membrane, or folding and release in the IMS.

Materials and Methods

Cloning of the Toc75-POTRA Constructs. For crystallization, the *A. thaliana* Toc75 sequence lacking the transit peptide was synthesized with codon optimization for bacterial expression (Bio Basic). Primers were designed to subclone residues 141–449 (POTRA1-3, including an N-terminal linker) into the pHIS-Parallel2 vector (containing an N-terminal 6×-HIS tag followed by a TEV protease site) for expression and purification. All cloning was verified using sequencing analysis at the Purdue Genomics Core Facility.

For cloning of POTRA1 for binding studies, the coding sequence of POTRA1 was cloned into pET21a to generate pET21a:POTRA1$_{His}$, encoding residues 140–247 of *Arabidopsis* Toc75 fused to a C-terminal hexahistidine tag. Codon-optimized versions of POTRA1-2 (residues 140–365 of Toc75), POTRA2-3 (residues 247–449 of Toc75), and POTRA3 were synthesized and cloned into pET28a (GenScript) to generate pET28a:POTRA1-2$_{His}$, pET28a:POTRA2-3$_{His}$, and pET28a:POTRA3$_{His}$, respectively, each with a C-terminal hexahistidine tag. POTRA2 was subcloned from the codon-optimized pHIS2:POTRA1-3 to pET21a to generate pET21a:POTRA2$_{His}$, encoding residues 247–365 of Toc75 fused to a C-terminal 6×-His tag.

Expression and Purification of POTRA1-3. Attempts to express natively folded POTRA1-3 were unsuccessful; therefore, refolding from inclusion bodies was performed. For crystallization, plasmids with POTRA1-3 were transformed into BL21(DE3)- competent cells, and a single colony used for a 5-mL starter culture of LB + 50 μg/mL ampicillin that was allowed to grow overnight. Aliquots of the starter culture were then added to 1 L of autoinduction TB medium using a modified Studier process (64, 65) (1 L Terrific Broth medium plus 50 mL of 20× NPS buffer and 25 mL of 50× 5052 medium, plus ampicillin) and allowed to grow for 2 d at 37 °C before cells were harvested. Cells were weighed and resuspended in 8 volumes of 1× PBS plus 1 mM PMSF, 1 mM BME, and 10 μg/mL Dnase I, then lysed by three passes through an Emulsiflex C3 homogenizer (Avestin). To isolate the inclusion bodies, cell lysate was centrifuged at 25,000 × *g* for 20 min at 4 °C, and supernatant was discarded. Inclusion bodies were then washed three times in 40 mL of 1× PBS by resuspending the pellet with a dounce homogenizer and then repelleted at 25,000 × *g* for 20 min at 4 °C. The inclusion bodies were then washed three times with 40 mL of 1× PBS + 1% Triton-X 100, and then resuspended in 40 mL of 1× PBS + 8 M urea. Debris was pelleted at 25,000 × *g* for 30 min at 4 °C. The supernatant was then dialyzed at 4 °C overnight against 2 L of 1× PBS, 1 mM PMSF, and 1 mM BME. The sample was then collected and pelleted at 25,000 × *g* for 20 min at 4 °C. The supernatant was then applied to a 5-mL nickel column on a AKTA Pure protein purification system (GE Healthcare) using 1× PBS, washed, and eluted using a gradient (0.02–1 M) of imidazole in 1× PBS. The peak fractions were verified by SDS/PAGE analysis, and all fractions were combined and treated with TEV protease to remove the 6×-His tag. This protease-treated sample was then passed over the nickel column a second time. The flow-through was concentrated and applied to

an S200 Sephacryl HR size exclusion column (GE Healthcare) using 1× PBS + 1 mM BME. Fractions containing POTRA protein were combined and concentrated to an approximate final concentration of ∼10 mg/mL.

POTRA1, POTRA1-2, POTRA2-3, POTRA2, and POTRA3 were expressed in BL21(DE3) cells with C-terminal hexahistidine tags. In brief, 1 L of LB with antibiotic was inoculated with ∼3 mL of overnight starter culture and grown to an OD_{600} of 0.6–0.8. Protein expression was induced with 1 mM isopropyl β-D-1-thiogalactopyranoside at 37 °C for 3 h or overnight at 23 °C. Cells were harvested by centrifugation at 8,000 × *g* for 15 min and lysed using a Cell Disruptor (Constant Systems) and/or 200 μg/mL lysozyme with sonication. For purification of POTRA1, cells were lysed in 20 mM Tris·HCl pH 8.0, 150 mM NaCl, and 10 mM imidazole, and soluble $POTRA1_{His}$ in the cleared lysate was bound to Ni-NTA His-Bind resin (Novagen), washed with HMK buffer (50 mM Hepes-KOH pH 7.5, 2 mM $MgCl_2$, and 40 mM KOAc) or PBS, and then eluted in HMK buffer (for solid-phase binding assays) or PBS (for insulin aggregation assay) with ∼100–250 mM imidazole. POTRA1-2, POTRA2-3, POTRA2, and POTRA3, were expressed as inclusion bodies. Inclusion bodies were washed three times with 25 mM Tris·HCl pH 8, 10 mM EDTA, 50 mM tryptone glucose extract (TGE) with 1% Triton X-100, and once with TGE without Triton X-100, then dissolved in binding buffer (20 mM Tris·HCl pH 8, 150 mM NaCl, and 10 mM imidazole) with 8 M urea and bound to Ni-NTA resin. Bound protein was refolded on the column by washing with 10 column volumes of a linear 8 M (in binding buffer) to 0 M (in HMK buffer or PBS) urea gradient, washed with HMK buffer or PBS, and eluted in HMK buffer or PBS with ∼100–250 mM imidazole. Elution fractions in HMK buffer were used directly for in vitro solid-phase binding assays. For insulin aggregation assays, eluted protein was dialyzed in PBS to remove imidazole and then concentrated using an Ultracel centrifugal filter with a 10-kDa cutoff (Centricon).

Analytical Ultracentrifugation. All experiments were conducted at 20 °C with a Beckman Coulter Optima XL-A analytical ultracentrifuge equipped with a four-hole An60Ti rotor and cells with 12-mm double-sector Epon centerpieces and quartz windows. POTRA1-3 was dialyzed overnight in 1× PBS. Sedimentation velocity experiments were conducted using 0.4 mL of sample volume. The centrifuge rotor was accelerated to 50,000 rpm after thermal equilibrium was reached at rest. Absorbance scans at 280 or 230 nm were started immediately after the rotor reached the set speed and continued until no further sedimentation boundary movement was observed. Partial specific volume of POTRA1-3, buffer density, and viscosity were calculated using the SEDNTERP program (sednterp.unh.edu/). Data analysis was conducted using the c(s) method in the SEDFIT program (66). The same software was used to calculate weight average sedimentation coefficients from distributions and to correct the sedimentation coefficients to standard conditions, s20,w.

SEC-SAXS. Data were recorded at beamline 18-ID of the Biophysics Collaborative Access Team at the Advanced Photon Source, Argonne National Laboratory, on a Pilatus3 1M detector (Dectris) covering a momentum transfer (*q*) range of 0.0036 to ∼0.4 $Å^{-1}$. An aliquot of POTRA1-3 at 2.0 mg/mL was injected onto an SEC column (Superdex 200 GL 10/300 Increase). SAXS data were recorded by exposing the column eluate to the X-ray beam for 1 s with a periodicity of 2 s. The SAXS signals from parts of the diffraction curve immediately preceding the sample elution peak were selected, averaged, and subtracted as the buffer blank from data points within the peak corresponding to POTRA1-3. Data analysis was performed at the beamline using various programs within the ATSAS program suite (67). Data were processed using PRIMUS (68), and R_g values was calculated from Guinier extrapolation. The pair distribution function P(r), calculated by Fourier inversion of the scattering intensity *I*(*q*) using GNOM (69), was used to calculate the R_g and D_{max} values. The results from GNOM were also used as an input in DAMMIF for reconstruction of an ab initio envelope (70). The resulting bead models were sequentially analyzed using DAMSEL, DAMSUP, and DAMAVER and then filtered using DAMMFILT (71). CRYSOL (72) was used to fit and compare theoretical scattering curves with the experimental SAXS curve. The POTRA1-3 crystal structure was then fit into the ab initio envelope using SUPCOMB (73).

Crystallization and Structure Determination. For crystallization, POTRA1-3 was concentrated to ∼10 mg/mL, and broad matrix crystallization screening was performed using a mosquito-LCP high throughput crystallization robot (TTP LabTech), and lead conditions were further optimized using a dragonfly screen optimization robot (TTP LabTech). The best crystals grew within ∼3 d at 12 °C in 100 mM Mes pH 5.0 and 10% PEG 6000 (space group $P2_1$) and 100 mM Hepes:NaOH pH 7.5 and 20% PEG 8000 (space group $P2_12_12_1$). Cryo solutions of 10% glycerol and 20% PEG 8000 were used during crystal harvesting and flash cooling into liquid nitrogen, respectively.

The initial POTRA1-3 structure was solved using the Se-SAD method with data collected on a single crystal at wavelength 0.9793 Å at beamline 8.2.2 at the Advanced Light Source, Lawrence Berkeley National Laboratory. The data were processed with Xia2 (74), and eight selenium sites were located and phasing was performed with AutoSol (PHENIX) (75), producing a figure of merit of 0.27/0.71 before/after density modification with a BAYES-CC of 37.5, an R-factor of 0.2956, and a map skew of 0.15. An initial model was built using AutoBuild (PHENIX) to ∼50% completeness, with the remainder of the model built manually. Subsequent structures were then solved by molecular replacement, with the initial model as a search model, using Phaser-MR (PHENIX) (75, 76). The highest-resolution dataset (2.5 Å) was collected at the SER-CAT beamline at the Advanced Photon Source, Argonne National Laboratory. All model building was performed using Coot (77), and subsequent refinement was done in PHENIX (75). Structure factors and model coordinates have been deposited in the Protein Data Bank (ID codes 5UAY and 5UBC). Electrostatic surface properties (calculated using the linearized Poisson–Boltzman equation mode with a solvent radius of 1.4) were analyzed and visualized using the APBS plug-in within PyMOL (Schrödinger). Molecular lipophilicity potential was calculated using VASCo (78) and visualized with the VASCo Surface Loader plug-in in PyMOL. Structure-related figures were created with PyMOL and annotated and finalized with Adobe Photoshop and Illustrator.

Solid-Phase Binding Assays. Solid-phase binding assays were carried out essentially as described previously (15). In brief, [^{35}S]-labeled prey was generated using an in vitro coupled transcription/translation kit according to the manufacturer's instructions (Promega). Radiolabeled in vitro translation products (IVTs) were subjected to SDS/PAGE, followed by phosphorimaging analysis using a Bio-Rad Personal Molecular Imager to measure relative translation efficiencies. Signals were quantitated by band densitometry using QuantityOne software (Bio-Rad). Indicated amounts of purified POTRAs diluted in HMK buffer to an imidazole concentration of ∼10 mM or less was immobilized on 10 μL of packed Ni-NTA His-Bind resin (Novagen) for 2 h at room temperature. Resin was washed once with HMK buffer with 10 mM imidazole and 0.1% Triton X-100 (HMKIT) or, in the case of [^{35}S]preSSU-DHFR (transit peptide of pea SSU fused to DHFR) experiments, with HMKIT with 100 mM KOAc. Radiolabeled IVT ([^{35}S]preSSU, [^{35}S]SSU, [^{35}S]preSSU-DHFR, or [^{35}S]DHFR) was added to immobilized POTRAs at equimolar amounts, determined by correcting the IVT signal of each substrate for the number of methionine residues and its relative molecular weight. Between 1 and 5 μL of IVT was added to each reaction (i.e., 5 μL of [^{35}S]SSU was used and ∼1–3 μL of other substrates were used depending on their corrected IVT signal). Reactions were incubated at room temperature for 2 h. Resin was washed three times with ice-cold HMKIT (or HMKIT with 100 mM KOAc in [^{35}S]preSSU-DHFR experiments), and bound protein was eluted in SDS/PAGE sample buffer containing 0.5 M imidazole. Samples were subjected to SDS/PAGE and phosphorimaging analysis, and binding was calculated as a percentage of the initial amount of radiolabeled prey added to the reaction after subtraction of background binding (1–3%).

Insulin Aggregation Assay. The insulin aggregation assay was performed essentially as described by Glaser et al. (42). In a 96-well plate, a total reaction volume of 100 μL was prepared with 35 μM insulin together with POTRA1-3, POTRA1, POTRA1-2, or POTRA2-3 at a 1:1 or 1:2 molar ratio of insulin: POTRAs in PBS. DTT was added to each reaction to a final concentration of 20 mM to initiate aggregation of insulin B. Insulin B aggregation over time was monitored by measuring the absorbance at 360 nm with a Spectramax microplate reader (Molecular Devices) at 25 °C while shaking. Light scattering of insulin in the presence of POTRAs was normalized to that of insulin, with 20 mM DTT in the absence of POTRAs as a control. As a negative control, light scattering of insulin B was measured in the absence of DTT. Experiments were done in triplicate, and data were averaged and smoothed using GraphPad Prism using a 10-neighbor average with a second-order smoothing polynomial and then plotted in Excel (Microsoft).

ACKNOWLEDGMENTS. We thank the staff at the Southeast Regional Collaborative Access Team (SER-CAT) and the Biophysics Collaborative Access Team (BioCAT) beamlines at the Advanced Photon Source, Argonne National Laboratory for their assistance. We also thank the staff at beamline 8.2.2 at the Advanced Light Source, Lawrence Berkeley National Laboratory for their assistance. Use of the Advanced Photon Source was supported by the US Department of Energy, Office of Science, Office of Basic Energy Sciences, under Contract W-31-109-Eng-38 (SER-CAT), and by a grant from the National Institute of General Medical Sciences (9 P41 GM103622) (BioCAT). Use of the Pilatus3 1M detector at BioCAT was provided by Grant 1S10OD018090-01 from the National Institute of General Medical Sciences.

The Berkeley Center for Structural Biology is supported in part by the National Institutes of Health, National Institute of General Medical Sciences, and the Howard Hughes Medical Institute. The Advanced Light Source is supported by the Director, Office of Science, Office of Basic Energy Sciences, of the US Department of Energy under Contract DE-AC02-05CH11231. P.K.O. and N.N. are supported by the Department of Biological Sciences at Purdue University, a Showalter Trust Award, and the National Institute of Allergy and Infectious Diseases (Grant 1K22AI113078-01). L.G.L.R., Y.D.P., and D.S. are supported by National Institutes of Health Grant 2R01 GM061893 (to D.S.). L.G.L.R. is supported by a postdoctoral fellowship from the Natural Sciences and Engineering Research Council of Canada.

1. Reyes-Prieto A, Weber AP, Bhattacharya D (2007) The origin and establishment of the plastid in algae and plants. *Annu Rev Genet* 41:147–168.
2. Keeling PJ (2013) The number, speed, and impact of plastid endosymbioses in eukaryotic evolution. *Annu Rev Plant Biol* 64:583–607.
3. Keeling PJ (2004) Diversity and evolutionary history of plastids and their hosts. *Am J Bot* 91:1481–1493.
4. Kalanon M, McFadden GI (2008) The chloroplast protein translocation complexes of *Chlamydomonas reinhardtii*: A bioinformatic comparison of Toc and Tic components in plants, green algae and red algae. *Genetics* 179:95–112.
5. Paila YD, Richardson LG, Schnell DJ (2015) New insights into the mechanism of chloroplast protein import and its integration with protein quality control, organelle biogenesis and development. *J Mol Biol* 427:1038–1060.
6. Hinnah SC, Hill K, Wagner R, Schlicher T, Soll J (1997) Reconstitution of a chloroplast protein import channel. *EMBO J* 16:7351–7360.
7. Hinnah SC, Wagner R, Sveshnikova N, Harrer R, Soll J (2002) The chloroplast protein import channel Toc75: Pore properties and interaction with transit peptides. *Biophys J* 83:899–911.
8. Kessler F, Schnell DJ (2004) Chloroplast protein import: Solve the GTPase riddle for entry. *Trends Cell Biol* 14:334–338.
9. Wallas TR, Smith MD, Sanchez-Nieto S, Schnell DJ (2003) The roles of toc34 and toc75 in targeting the toc159 preprotein receptor to chloroplasts. *J Biol Chem* 278: 44289–44297.
10. Tu SL, et al. (2004) Import pathways of chloroplast interior proteins and the outer-membrane protein OEP14 converge at Toc75. *Plant Cell* 16:2078–2088.
11. Sohrt K, Soll J (2000) Toc64, a new component of the protein translocon of chloroplasts. *J Cell Biol* 148:1213–1221.
12. Qbadou S, et al. (2006) The molecular chaperone Hsp90 delivers precursor proteins to the chloroplast import receptor Toc64. *EMBO J* 25:1836–1847.
13. Hsu SC, Inoue K (2009) Two evolutionarily conserved essential β-barrel proteins in the chloroplast outer envelope membrane. *Biosci Trends* 3:168–178.
14. Eckart K, et al. (2002) A Toc75-like protein import channel is abundant in chloroplasts. *EMBO Rep* 3:557–562.
15. Paila YD, et al. (2016) Multi-functional roles for the polypeptide transport associated domains of Toc75 in chloroplast protein import. *eLife* 5:5.
16. Töpel M, Ling Q, Jarvis P (2012) Neofunctionalization within the Omp85 protein superfamily during chloroplast evolution. *Plant Signal Behav* 7:161–164.
17. Day PM, Potter D, Inoue K (2014) Evolution and targeting of Omp85 homologs in the chloroplast outer envelope membrane. *Front Plant Sci* 5:535.
18. Patel R, Hsu SC, Bédard J, Inoue K, Jarvis P (2008) The Omp85-related chloroplast outer envelope protein OEP80 is essential for viability in *Arabidopsis*. *Plant Physiol* 148:235–245.
19. Inoue K, Potter D (2004) The chloroplastic protein translocation channel Toc75 and its paralog OEP80 represent two distinct protein families and are targeted to the chloroplastic outer envelope by different mechanisms. *Plant J* 39:354–365.
20. Schleiff E, Maier UG, Becker T (2011) Omp85 in eukaryotic systems: One protein family with distinct functions. *Biol Chem* 392:21–27.
21. Voulhoux R, Tommassen J (2004) Omp85, an evolutionarily conserved bacterial protein involved in outer-membrane-protein assembly. *Res Microbiol* 155:129–135.
22. Ulrich T, Rapaport D (2015) Biogenesis of β-barrel proteins in evolutionary context. *Int J Med Microbiol* 305:259–264.
23. Noinaj N, Rollauer SE, Buchanan SK (2015) The β-barrel membrane protein insertase machinery from Gram-negative bacteria. *Curr Opin Struct Biol* 31:35–42.
24. Paschen SA, Neupert W, Rapaport D (2005) Biogenesis of beta-barrel membrane proteins of mitochondria. *Trends Biochem Sci* 30:575–582.
25. Simmerman RF, Dave AM, Bruce BD (2014) Structure and function of POTRA domains of Omp85/TPS superfamily. *Int Rev Cell Mol Biol* 308:1–34.
26. Kim S, et al. (2007) Structure and function of an essential component of the outer membrane protein assembly machine. *Science* 317:961–964.
27. Bennion D, Charlson ES, Coon E, Misra R (2010) Dissection of β-barrel outer membrane protein assembly pathways through characterizing BamA POTRA 1 mutants of *Escherichia coli*. *Mol Microbiol* 77:1153–1171.
28. Gu Y, et al. (2016) Structural basis of outer membrane protein insertion by the BAM complex. *Nature* 531:64–69.
29. Stroud DA, et al. (2011) Biogenesis of mitochondrial β-barrel proteins: The POTRA domain is involved in precursor release from the SAM complex. *Mol Biol Cell* 22: 2823–2833.
30. Bohnert M, et al. (2012) Role of mitochondrial inner membrane organizing system in protein biogenesis of the mitochondrial outer membrane. *Mol Biol Cell* 23: 3948–3956.
31. Chen YL, Chen LJ, Li HM (2016) Polypeptide transport-associated domains of the Toc75 channel protein are located in the intermembrane space of chloroplasts. *Plant Physiol* 172:235–243.
32. Jackson-Constan D, Keegstra K (2001) *Arabidopsis* genes encoding components of the chloroplastic protein import apparatus. *Plant Physiol* 125:1567–1576.
33. Baldwin A, et al. (2005) A molecular-genetic study of the *Arabidopsis* Toc75 gene family. *Plant Physiol* 138:715–733.
34. Hust B, Gutensohn M (2006) Deletion of core components of the plastid protein import machinery causes differential arrest of embryo development in *Arabidopsis thaliana*. *Plant Biol (Stuttg)* 8:18–30.
35. Gruss F, et al. (2013) The structural basis of autotransporter translocation by TamA. *Nat Struct Mol Biol* 20:1318–1320.
36. Noinaj N, et al. (2013) Structural insight into the biogenesis of β-barrel membrane proteins. *Nature* 501:385–390.
37. Bakelar J, Buchanan SK, Noinaj N (2016) The structure of the β-barrel assembly machinery complex. *Science* 351:180–186.
38. Han L, et al. (2016) Structure of the BAM complex and its implications for biogenesis of outer-membrane proteins. *Nat Struct Mol Biol* 23:192–196.
39. Gatzeva-Topalova PZ, Walton TA, Sousa MC (2008) Crystal structure of YaeT: Conformational flexibility and substrate recognition. *Structure* 16:1873–1881.
40. Gatzeva-Topalova PZ, Warner LR, Pardi A, Sousa MC (2010) Structure and flexibility of the complete periplasmic domain of BamA: The protein insertion machine of the outer membrane. *Structure* 18:1492–1501.
41. Ertel F, et al. (2005) The evolutionarily related β-barrel polypeptide transporters from *Pisum sativum* and Nostoc PCC7120 contain two distinct functional domains. *J Biol Chem* 280:28281–28289.
42. Glaser S, et al. (2012) Tic22 is an essential chaperone required for protein import into the apicoplast. *J Biol Chem* 287:39505–39512.
43. Maier T, et al. (2015) Conserved Omp85 lid-lock structure and substrate recognition in FhaC. *Nat Commun* 6:7452.
44. Albrecht R, et al. (2014) Structure of BamA, an essential factor in outer membrane protein biogenesis. *Acta Crystallogr D Biol Crystallogr* 70:1779–1789.
45. Ni D, et al. (2014) Structural and functional analysis of the β-barrel domain of BamA from *Escherichia coli*. *FASEB J* 28:2677–2685.
46. Clantin B, et al. (2007) Structure of the membrane protein FhaC: A member of the Omp85-TpsB transporter superfamily. *Science* 317:957–961.
47. Iadanza MG, et al. (2016) Lateral opening in the intact β-barrel assembly machinery captured by cryo-EM. *Nat Commun* 7:12865.
48. Knowles TJ, et al. (2008) Fold and function of polypeptide transport-associated domains responsible for delivering unfolded proteins to membranes. *Mol Microbiol* 68: 1216–1227.
49. Koenig P, et al. (2010) Conserved properties of polypeptide transport-associated (POTRA) domains derived from cyanobacterial Omp85. *J Biol Chem* 285:18016–18024.
50. Arnold T, Zeth K, Linke D (2010) Omp85 from the thermophilic cyanobacterium *Thermosynechococcus elongatus* differs from proteobacterial Omp85 in structure and domain composition. *J Biol Chem* 285:18003–18015.
51. Balsera M, Soll J, Buchanan BB (2010) Redox extends its regulatory reach to chloroplast protein import. *Trends Plant Sci* 15:515–521.
52. Rollauer SE, Sooreshjani MA, Noinaj N, Buchanan SK (2015) Outer membrane protein biogenesis in Gram-negative bacteria. *Philos Trans R Soc Lond B Biol Sci* 370:20150023.
53. Knowles TJ, Scott-Tucker A, Overduin M, Henderson IR (2009) Membrane protein architects: The role of the BAM complex in outer membrane protein assembly. *Nat Rev Microbiol* 7:206–214.
54. Ricci DP, Silhavy TJ (2012) The Bam machine: A molecular cooper. *Biochim Biophys Acta* 1818:1067–1084.
55. Selkrig J, et al. (2012) Discovery of an archetypal protein transport system in bacterial outer membranes. *Nat Struct Mol Biol* 19:506–510.
56. Jacob-Dubuisson F, Villeret V, Clantin B, Delattre AS, Saint N (2009) First structural insights into the TpsB/Omp85 superfamily. *Biol Chem* 390:675–684.
57. Bruce BD (2001) The paradox of plastid transit peptides: Conservation of function despite divergence in primary structure. *Biochim Biophys Acta* 1541:2–21.
58. Endo T, Kawamura K, Nakai M (1992) The chloroplast-targeting domain of plastocyanin transit peptide can form a helical structure but does not have a high affinity for lipid bilayers. *Eur J Biochem* 207:671–675.
59. Wienk HL, Czisch M, de Kruijff B (1999) The structural flexibility of the preferredoxin transit peptide. *FEBS Lett* 453:318–326.
60. Zhang XC, Han L (2016) How does a β-barrel integral membrane protein insert into the membrane? *Protein Cell* 7:471–477.
61. Kouranov A, Chen X, Fuks B, Schnell DJ (1998) Tic20 and Tic22 are new components of the protein import apparatus at the chloroplast inner envelope membrane. *J Cell Biol* 143:991–1002.
62. Kasmati AR, et al. (2013) Evolutionary, molecular and genetic analyses of Tic22 homologues in *Arabidopsis thaliana* chloroplasts. *PLoS One* 8:e63863.
63. Rudolf M, et al. (2013) In vivo function of Tic22, a protein import component of the intermembrane space of chloroplasts. *Mol Plant* 6:817–829.
64. Studier FW (2014) Stable expression clones and auto-induction for protein production in *E. coli*. *Methods Mol Biol* 1091:17–32.
65. Studier FW (2005) Protein production by auto-induction in high-density shaking cultures. *Protein Expr Purif* 41:207–234.
66. Schuck P (2000) Size-distribution analysis of macromolecules by sedimentation velocity ultracentrifugation and Lamm equation modeling. *Biophys J* 78:1606–1619.
67. Petoukhov MV, et al. (2012) New developments in the ATSAS program package for small-angle scattering data analysis. *J Appl Cryst* 45:342–350.

68. Konarev PV, Volkov VV, Sokolova AV, Koch MHJ, Svergun DI (2003) PRIMUS: A Windows PC-based system for small-angle scattering data analysis. *J Appl Cryst* 36:1277–1282.
69. Svergun D (1992) Determination of the regularization parameter in indirect-transform methods using perceptual criteria. *J Appl Cryst* 25:495–503.
70. Franke D, Svergun DI (2009) DAMMIF, a program for rapid ab-initio shape determination in small-angle scattering. *J Appl Cryst* 42:342–346.
71. Volkov VV, Svergun DI (2003) Uniqueness of ab initio shape determination in small-angle scattering. *J Appl Cryst* 36:860–864.
72. Svergun D, Barberato C, Koch MHJ (1995) CRYSOL: A program to evaluate X-ray solution scattering of biological macromolecules from atomic coordinates. *J Appl Cryst* 28:768–773.
73. Kozin MB, Svergun DI (2001) Automated matching of high- and low-resolution structural models. *J Appl Cryst* 34:33–41.
74. Winter G (2010) xia2: An expert system for macromolecular crystallography data reduction. *J Appl Cryst* 43:186–190.
75. Adams PD, et al. (2010) PHENIX: A comprehensive Python-based system for macromolecular structure solution. *Acta Crystallogr D Biol Crystallogr* 66:213–221.
76. McCoy AJ, et al. (2007) Phaser crystallographic software. *J Appl Cryst* 40:658–674.
77. Emsley P, Lohkamp B, Scott WG, Cowtan K (2010) Features and development of Coot. *Acta Crystallogr D Biol Crystallogr* 66:486–501.
78. Steinkellner G, Rader R, Thallinger GG, Kratky C, Gruber K (2009) VASCo: Computation and visualization of annotated protein surface contacts. *BMC Bioinformatics* 10:32.